Isotope dependent, temperature regulated, energy repartitioning in a low-barrier, short-strong hydrogen bonded cluster

Xiaohu Li,[1] Jos Oomens,[2] John R. Eyler,[3] David T. Moore,[4,a)] and Srinivasan S. Iyengar[1,5,a)]

[1]*Department of Chemistry, Indiana University, 800 E. Kirkwood Ave., Bloomington, Indiana 47405, USA*
[2]*FOM Institute for Plasma Physics 'Rijnhuizen', Edisonbaan 14, 3439 MN Nieuwegein, The Netherlands*
[3]*Department of Chemistry, University of Florida, Gainesville, Florida 32611, USA*
[4]*Department of Chemistry, Lehigh University, Bethlehem, Pennsylvania 18015, USA*
[5]*Department of Physics, Indiana University, 727 E. Third St., Bloomington, Indiana 47405, USA*

We investigate and analyze the vibrational properties, including hydrogen/deuterium isotope effects, in a fundamental organic hydrogen bonded system using multiple experimental (infrared multiple photon dissociation and argon-tagged action spectroscopy) and computational techniques. We note a qualitative difference between the two experimental results discussed here and employ *ab initio* molecular dynamics simulations to explain these results. A deeper understanding of the differences between the isotopically labeled systems arises from an analysis of the simulated cluster spectroscopy and leads to a system-bath coupling interpretation. Specifically, when a few active modes, involving the shared hydrogen/deuterium stretch, are identified and labeled as "system," with all other molecular vibrational modes being identified as "bath" modes, we find critical differences in the coupling between the system modes for the shared proton and shared deuteron cases. These differences affect the energy repartitioning between these modes resulting in a complex spectral evolution as a function of temperature. Furthermore, intensity borrowing across modes that are widely distributed in the frequency domain plays an important role on the simulated spectra. © *2010 American Institute of Physics*. [doi:10.1063/1.3430525]

I. INTRODUCTION

Hydrogen bonds and hydrogen transfer systems have a fundamental role in many biological,[1] materials,[2,3] and atmospheric[4–9] processes. Experimentally, H/D isotope substitution is often used as a tool to probe these systems. In addition, there are many instances where temperature-dependent primary and secondary isotope effects have been recorded on hydrogen bonded and hydrogen transfer systems to yield novel mechanistic insights.[1,3]

Here, we study a fundamental organic shared H/D system: a charged species that contains a short-strong hydrogen bond[10–17] involving a proton or deuteron bound to two organic ethers, namely, $[R_2O-H-OR_2]^+$ and its deuterated analog $[R_2O-D-OR_2]^+$, using multiple experimental and computational techniques. Similar low-barrier, short-strong hydrogen bonds have been widely explored with respect to significance in many enzyme catalytic reactions.[10–17] Furthermore, when the R-group is a hydrogen atom, the system studied represents the well-known Zundel cation,[18–21] which is a low-barrier hydrogen bonded complex that plays an important role in proton transfer in condensed phase systems. The critical interactions involved in such systems are also seen in many host-guest systems.[22] Similar systems have

also been utilized as models to understand secondary isotope effects in enzymes.[23] We inspect the factors that determine the vibrational properties by considering isotope substitution as well as temperature effects. Our analysis is based on experimental infrared multiple photon dissociation[20,24–29] (IRMPD) and previously conducted argon-tagged single photon action spectroscopy studies.[7] These experimental results are supported through facilitating finite temperature *ab initio* molecular dynamics (AIMD) simulations.[30–32] The experimental techniques are both action spectroscopy methods and differ in the ion temperature and method of measurement. While the IRMPD uses noncoherent multiple photons with room-temperature ions, the argon-tagged measurement is a single photon process with cold ions.

We note, what appears to be, a qualitative difference between the experimental results for the deuterated species, $[Me_2O-D-OMe_2]^+$. While the argon-tagged spectrum[7] is in reasonable agreement with the harmonic frequencies obtained from electronic structure calculations, the IRMPD spectral results are broad and appear to be very different. Finite temperature AIMD simulations constructed using a single (ground) electronic potential surface provide good agreement with both experimental results and are utilized here to unravel the energy distributions and mode couplings responsible for the differences between the two experimental results. In a nutshell, the vibrational properties of the deuter-

a)Electronic addresses: iyengar@indiana.edu and david.moore@lehigh.edu.

ated system are dictated by coupling between modes that combine the shared deuteron stretch and ether backbone stretch. By comparison, the protonated species displays interactions between the shared proton stretch, the ether backbone symmetric stretch, and other vibrational modes of the molecule. This difference, along with its temperature-dependent modulation, explains a critical portion of the spectral differences between the protonated and deuterated systems and also the results from the two experiments. As far as we are aware, this is also the first time this level of concordance between these experimental techniques (IRMPD and argon-tagged action spectroscopy) and theory has been reached for a set of spectra of a hydrogen-bound system, incorporating both a wide temperature range and isotopic effects.

The paper is organized as follows: In Sec. II the experimental and computational methods are described. Section III provides a discussion on the temperature dependence of the vibrational properties whereas in Secs. IV and V we analyze the role of energy redistribution. Conclusions are given in Sec. VI.

II. EXPERIMENTAL AND COMPUTATIONAL METHODS

A. Infrared multiple photon dissociation spectroscopy and argon-tagged action spectroscopy

The IRMPD spectroscopy was carried out using a Fourier transform ion cyclotron resonance (FTICR) mass-spectrometer interfaced with the infrared free-electron laser (FELIX) facility in the Netherlands; this apparatus has been discussed in detail elsewhere.[27] Briefly, the deuteron-bound methyl ether dimers were created *in situ* inside the FTICR cell, and then irradiated with tunable IR light from FELIX. First, D_3O^+ ions were created from D_2O vapor ($\approx 10^{-7}$ torr) by electron impact ionization followed by ion-molecule reactions. Methyl ether vapor was then admitted from a pulsed valve (peak pressure $\approx 10^{-6}$ torr) and the deuteron-bound dimer was formed in a stepwise fashion from ion-molecule reactions, first D^+-transfer to form deuterated methyl ether monomer $[Me_2OD^+]$, followed by capture of a second methyl ether to form the dimer $[Me_2O-D-OMe_2]^+$. The dimers were then isolated in the trap and stored for 1 s to allow them to reach radiative thermal equilibrium with the room-temperature cell.[28] Several (five to ten) IR pulses from the free-electron laser were then used to irradiate the ions while monitoring fragmentation signal in the m/z=48 mass channel, corresponding to $[Me_2OD^+]$. IRMPD spectra, represented as the ratio of fragment ion signal to total ion signal, were recorded by repeating this sequence while scanning the laser wavelength. The reported intensities have been normalized to account for the power spectrum of the FELIX laser. It should be noted that no significant fragmentation into other mass channels was observed, and in particular, no signal was observed in the m/z=47 channel. This rules out contributions to the spectrum from structural isomers where the deuteron was exchanged with a methyl hydrogen to create a proton-bound,

monodeuterated species. Such parent ions would show competitive fragmentation into the m/z=48 or m/z=47 channels so the absence of significant signal in the m/z=47 channel strongly suggests that such isomers are not reflected in the spectrum.

In addition, as outlined in Ref. 31, these are noncoherent multiple photon dissociation processes. For the IRMPD spectra presented here, and indeed in most other cases studied, the scaling of the measured intensities with laser power is linear,[33–35] which is a strong indication that only single photon processes are responsible for the observed spectra. Indeed, in Refs. 28, 33, and 35 it has been shown that the peak positions (frequencies) are in agreement with calculated spectra obtained from geometry optimization and harmonic frequency calculations, and with measured spectra obtained with other means.[28,33,35] Furthermore, in Ref. 31, $[Me_2O-H-OMe_2]^+$ has been studied using AIMD simulations at two different temperatures and the resultant spectra have been shown to qualitatively agree with IRMPD. Since the systems treated in this publication are quite similar to those studied in Refs. 28 and 31, one would expect a similar trend here as well.

The argon-tagged spectra shown here are from Ref. 7. For completeness we provide a brief overview of this experiment, with details in Refs. 7 and 36. Briefly, these spectra were recorded by the group of Johnson[7] using their cluster-ion spectroscopy apparatus. Electronic versions of these spectra were provided to us by the group of Johnson (see acknowledgments). The argon-tagging method is a type of vibrational predissociation spectroscopy, whereby argon atoms are attached to molecular or cluster ions in a cold molecular beam, and then resonantly detached by using an infrared laser to excite vibrations within the ion cluster. The vibrational spectra were obtained by scanning the laser frequency while monitoring the argon-loss fragmentation channel in a mass spectrometer. Since the binding energy of an argon atom to the cluster is quite small, the dissociation thresholds for argon-tagged systems are much lower than for IRMPD, and a single infrared photon typically carries enough energy to dissociate the clusters.

B. Computational methods

A large number of simulations have been conducted as part of our study employing the AIMD techniques, Born–Oppenheimer molecular dynamics (BOMD),[37–39] and atom-centered density matrix propagation (ADMP),[9,40–43] as implemented within a development version of the Gaussian series of electronic structure codes.[44] These simulations utilize the B3LYP hybrid density functional with double-zeta polarized-diffused 6-31+G** basis, as suggested from previous studies[9,30,32,45–49] on similar systems. Geometry optimization and harmonic frequency calculations, at density functional as well as post-Hartree–Fock (MP2) levels are performed to assist the decomposition and assignment of spectra obtained from AIMD simulations.

The AIMD simulations conducted here are similar in nature to those utilized in Refs. 30–32. Briefly, all systems considered here are treated as gas-phase clusters to remain

TABLE I. Simulation parameters: temperature fluctuations in the AIMD and microcanonical ensemble (NVE) simulations. All simulations shown are 15 ps in length.

$[Me_2O-H-OMe_2]^+$		$[Me_2O-D-OMe_2]^+$	
Temperature[a]	ΔE [b]	Temperature[a]	ΔE [b]
39 K ± 6 K	0.009	39 K ± 6 K	0.007
68 K ± 10 K	0.013	68 K ± 11 K	0.014
109 K ± 15 K	0.040	109 K ± 16 K	0.030
273 K ± 39 K	0.194	272 K ± 39 K	0.176
392 K ± 54 K	0.160	390 K ± 56 K	0.115

[a]Average temperature and fluctuations for all the AIMD and NVE simulations (in Kelvin).
[b]rms deviation in the total energy during simulation (kcal/mol). The angular momentum of the system is conserved at J=0 for all simulations, with fluctuations of the order $10^{-8}\hbar$.

consistent with the experimental work. A time step of 0.5 fs was chosen for all BOMD studies while a fictitious mass-tensor scaling value of 0.1 amu bohr^2 ($\approx$180 a.u.) and a time step of 0.25 fs was used for ADMP. The AIMD simulations conducted here are microcanonical (NVE), with acceptable fluctuations in the internal temperature (see Table I) and all nuclei are treated classically. Since time-correlation functions involving nuclear velocities as well as molecular dipoles are utilized to obtain vibrational properties, a constant energy simulation with an associated conservative Hamiltonian corresponding to the real system is critical. The total energy was well conserved in our simulations as noted in Table I. The total angular momentum of the classical nuclear system was also well conserved (with initial conditions corresponding to J=0) and residual angular forces, resulting from finite numerical precision, were projected out during the dynamics process. This also implies that any rotation-vibrational coupling effects are not included in the simulation. A body-fixed 3N-dimensional Cartesian coordinate system at the center-of-mass, which was conserved all through the dynamics, was used to represent nuclear positions and momenta. Many different sets of simulations were conducted, in the temperature range of 30–400 K, five of which are discussed in Sec. III to help understand the experimental results (also see Table I). The choice of temperature determines the distribution of initial kinetic energy and the corresponding phase-space distribution function. The temperature for these simulations was chosen as follows: Since the argon-tagged spectrum was recorded using low-temperature ions, we have computed a few trajectories under 100 K. This choice is consistent with the agreement seen between argon-tagged spectroscopy results and previous AIMD simulations.[30,45] Similarly, we computed trajectories at 273 ± 39 and 390 ± 55 K because the IRMPD experiments were performed using room-temperature ions.

The dynamically averaged vibrational spectra were computed by using the Fourier transform of the nuclear velocity autocorrelation function (FT-VAC) and Fourier transform of the dipole autocorrelation function (FT-DAC). The FT-VAC is defined as

$$
\begin{aligned}
I_V(\omega) &= \lim_{T\to\infty}\int_{t=0}^{t=T} dt\, \exp(-\iota\omega t)\langle \mathbf{V}(0)\cdot\mathbf{V}(t)\rangle \\
&= \lim_{T\to\infty}\sum_{i=1}^{N_{\text{atoms}}}\sum_{j=1}^{3}\int_{t=0}^{t=T} dt \\
&\quad\times\exp(-\iota\omega t)\int_{t'=0}^{t'=T} dt'\, V_{i,j}(t') * V_{i,j}(t'+t) \\
&= \lim_{T\to\infty}\sum_{i=1}^{N_{\text{atoms}}}\sum_{j=1}^{3}\left|\int_{t=0}^{t=T} dt\, \exp(-\iota\omega t) V_{i,j}(t)\right|^2, \quad (1)
\end{aligned}
$$

where the term $\langle\cdots\rangle$, in the first equation, indicates ensemble average and is equal to the t'-integral in the second equation under the ergodicity condition. We have used the convolution theorem[50] to reduce the second equation to the third equation. The FT-VAC provides the vibrational density of states.

The FT-DAC provides peak intensities proportional to the change in dipole moment of the system and the vibrational spectrum[30–32,45,51–55] inclusive of these intensities is computed as

$$
\begin{aligned}
\alpha_\mu^{QC}(\omega) &\propto \frac{\omega}{1-\exp(-\beta\hbar\omega)}\Bigg\{\omega[1-\exp(-\beta\hbar\omega)]\lim_{T\to\infty}\int_{t=0}^{t=T} dt \\
&\quad\times\exp(-\iota\omega t)\langle\boldsymbol{\mu}(0)\cdot\boldsymbol{\mu}(t)\rangle\Bigg\}.
\end{aligned} \quad (2)
$$

The terms inside the curly brackets ($\{\cdots\}$) represents the power normalized absorption cross section.[51,52] The prefactor, $\omega/[1-\exp(-\beta\hbar\omega)]$, is a quantum nuclear correction[53–55] obtained based on the harmonic approximation. Over a series of publications[30–32,36,45] it has been demonstrated that these correlation functions provide a good estimate to the vibrational spectrum obtained from experimental action spectroscopy. Utilizing the convolution theorem[50] as above, Eq. (2) may be rewritten as

$$
\alpha_\mu^{QC}(\omega) \propto \omega^2 \lim_{T\to\infty}\sum_{i=1}^{3}\left|\int_{t=0}^{t=T} dt\, \exp(-\iota\omega t)\mu_i(t)\right|^2. \quad (3)
$$

In this work, we have also computed the power normalized quantum nuclear corrected line shape,

$$
\begin{aligned}
I_\mu^{QC}(\omega) &\propto \frac{\omega}{1-\exp(-\beta\hbar\omega)}\Bigg\{\lim_{T\to\infty}\sum_{i=1}^{3}\left|\int_{t=0}^{t=T} dt\right. \\
&\quad\left.\times\exp(-\iota\omega t)\mu_i(t)\right|^2\Bigg\}.
\end{aligned} \quad (4)
$$

The spectral results from BOMD and ADMP are qualitatively similar and all data provided are from BOMD simulations. The value of T in Eqs. (1)–(4) is the length of simulation (15 ps) stated in Table I, which is much larger than the usual vibrational scale in gas phase. The convergence of the simulated spectra has been confirmed by considering different simulation lengths.
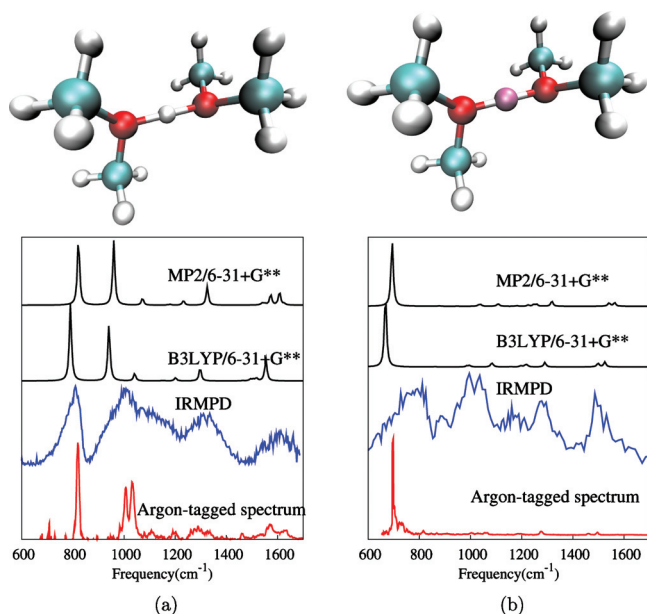
FIG. 1. The IRMPD (blue) and argon-tagged (red) action spectra for (a) $[Me_2O-H-OMe_2]^+$ and (b) $[Me_2O-D-OMe_2]^+$ are compared to computational results obtained here using harmonic approximation (black). (a) The experimental spectra are reproduced from Ref. 28 (IRMPD) and Ref. 7 (argon-tagged spectrum). (b) The argon-tagged result is reproduced from Ref. 7, while the IRMPD spectrum is obtained here. The two figures on top display the respective protonated and deuterated systems, where the bound deuteron is purple.

III. ANALYSIS OF VIBRATIONAL SPECTRAL BEHAVIOR

We begin by examining the four experimental spectra (blue and red traces) in Fig. 1. As noted in Sec. II, the ions in IRMPD are equilibrated to room temperature, whereas the system in the argon-tagged experiment is maintained at a much lower temperature. It is clear that the two low-temperature Ar-tagged spectra in Figs. 1(a) and 1(b) are qualitatively quite different. The deuteron-bound dimer spectrum consists of a single strong peak near 700 cm^{-1}, while the proton-bound dimer spectrum shows much more structure, with a strong peak near 800 cm^{-1}, a strong doubletlike feature near 1050 cm^{-1}, and some broad weak bands at higher frequencies. On the other hand, the two high-temperature IRMPD spectra of the protonated and deuterated species are qualitatively quite similar. The only significant differences are the broadening toward the low wavenumber limit and the peak near 900 cm^{-1} in the deuteron-bound dimer spectrum, as well as the shift of the band near the high-frequency limit from 1600 cm^{-1} (proton bound) to 1500 cm^{-1} (deuteron bound).

One can also make similar comparisons between the high- and low-temperature spectra for each species. In the proton-bound case, the high-temperature spectrum resembles a broader version of the low-temperature spectrum, with some shifts in relative band intensities. In contrast, for the deuteron-bound dimer, the high-temperature spectrum looks very different from the low-temperature spectrum, and in fact it is hard to see how both spectra could represent the same system. We have shown in Ref. 31 that the two proton-bound experimental spectra in Fig. 1(a) can be reproduced
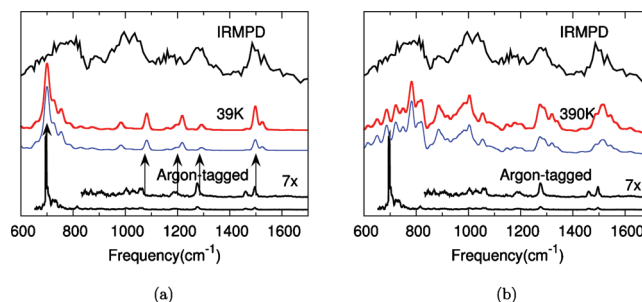

FIG. 2. (a) and (b) display the 39 and 390 K AIMD spectra for $[Me_2O-D-OMe_2]^+$, obtained using Eq. (3) (red) and Eq. (4) (blue). The experimental argon-tagged and IRMPD results are shown in black. Note that the argon-tagged results are reproduced well at 39 K. The 390 K AIMD spectra reproduce the IRMPD result.

from AIMD simulations using a single (ground-state) potential energy surface, changing only the simulation temperature. In this publication we find it to be the case for the deuteron-bound species as well. In addition, in Secs. IV A and IV B, we inspect energy redistribution pathways that lead to the complex temperature dependence of the spectra and distinguish these pathways between the protonated and deuterated systems.

Two of the AIMD simulation spectra for the deuteron-bound species are compared to the experimental spectra in Fig. 2. The black traces reproduce the experimental spectra from Fig. 1(b). The red and blue traces display the $\alpha_\mu^{QC}(\omega)$ intensities of Eq. (3) and $I_\mu^{QC}(\omega)$ intensities of Eq. (4), respectively, which are obtained from the AIMD simulations performed at 39 and 390 K. As noted earlier, Eqs. (3) and (4) provide intensities proportional to the change in dipole of the system. Furthermore, since these are constructed using finite temperature *ab initio* dynamics data, all potential energy surface parameters, including all anharmonicity contributions, are accounted for in this study. It is clear in both cases that the 39 and 390 K simulations produce good qualitative agreement with the low- (argon-tagged) and high-temperature (IRMPD) experimental spectra, respectively. The spectra obtained from Eq. (4) are a little lower in intensity as compared to those obtained from Eq. (3). This is to be expected based on the ω-dependent prefactors in these equations. While the prefactor in Eq. (3) is quadratic in ω, that in Eq. (4) is sublinear. [Note that the proportionality constants in Eqs. (2) and (3) include, the temperature, speed of light and Planck's constant. Since these are constants for a given simulation, they only contribute a uniform scaling to all spectra and are thus omitted from our discussion.] The 39 K simulation reproduces the strong feature at 700 cm^{-1} [Fig. 2(a)], which is assigned to the antisymmetric triatomic ODO stretch, based on the *ab initio* harmonic frequencies. The peak positions of several weaker features at higher wavenumber are also correctly reproduced in the 39 K spectrum, although the calculated intensities are higher than in the argon-tagged experiment.

In Ref. 7, the weak features at $\approx$800 and 1000 cm^{-1} in the deuteron-bound dimer spectrum have been suggested as possibly arising from overlapping bands from the ^{13}C-isotopologue of the proton-bound system. This analysis in Ref. 7 was based on calculations of harmonic frequencies

of the shared proton and deuteron systems, with the mass-selected experimental conditions that allow the formation of the ^{13}C-isotopologue of the proton-bound system with the ^{12}C-isotopologue of the deuteron-bound system. The conclusions in Ref. 7 were also based on the absence of spectral features in the corresponding regions of the harmonic deuterated spectrum. In Fig. 2(a), we show that the simulated AIMD spectrum at 39 K (which includes anharmonic effects as a result of potential energy sampling during AIMD simulations) predicts a band near 1050 cm^{-1}, which correlates with a band from Ref. 7, as indicated by an arrow in the figure. Since this region of the experimental spectrum is congested and may contain several overlapping bands, it is likely that the ^{13}C-isotopologue system as well as features found here for the ^{12}C-isotopologue contribute. The assignment of this region in the current work is provided in Table III and discussed as part of Sec. IV B. It is noted that this region has contributions from harmonic normal modes corresponding to the shared deuteron stretch coupled with the ether backbone (C–O–C) stretch and methyl group wag.

Similarly, the 390 K AIMD spectrum yields a qualitatively accurate reproduction of the positions, relative intensities, and bandwidths of the major features in the room-temperature IRMPD spectrum. Even some of the weaker features, such as the small bands near 900 and 1175 cm^{-1}, and the apparent shoulder on the blue edge of the 1300 cm^{-1} peak, are reproduced by the simulation. Since these results are obtained using a single electronic potential surface, it appears that the broadbands observed in IRMPD, through the use of incoherent multiple photons,[31] do represent a high-temperature form of the single photon spectrum.

It is interesting to consider the evolution of the spectrum as the temperature is increased from 39 to 390 K. Such a progression is presented in Fig. 3 for the shared deuteron case, where the $\alpha_\mu^{QC}(\omega)$ spectra at 68, 109, and 272 K have been added. [The $I_\mu^{QC}(\omega)$ results are also in similar agreement, but have relatively lower intensities in the higher frequency region consistent with those seen in Fig. 2.] Here, the experimental spectra are shown in black, the simulated spectra at 39 and 390 K, that are in close agreements with the experiments, are in red. Simulated spectra that interpose between the 39 and 390 K temperatures are shown in blue. The dominant effect at low temperature is a shift in intensity in the low frequency 600–860 cm^{-1} region. As the temperature is increased from 39 K, the predominant intensity contributions shift from the 665 cm^{-1} region toward higher frequencies as indicated by the broken arrow between 39 and 68 K. This trend then continues in the 109 and 272 K spectra, as other bands begin to fill in between 850 and 1050 cm^{-1}. As we see below, this effect arises from coupling between the shared deuteron stretch and the ether backbone symmetric stretch. The other important effects pertain to the general broadening and growth in the intensity of most peaks with increasing temperature. We analyze these differences in Sec. IV through a spectral decomposition of the finite temperature features.

A similar progression of spectra with temperature for the shared proton case is presented in Fig. 4. The results here differ from those in Ref. 31 in that additional temperature-
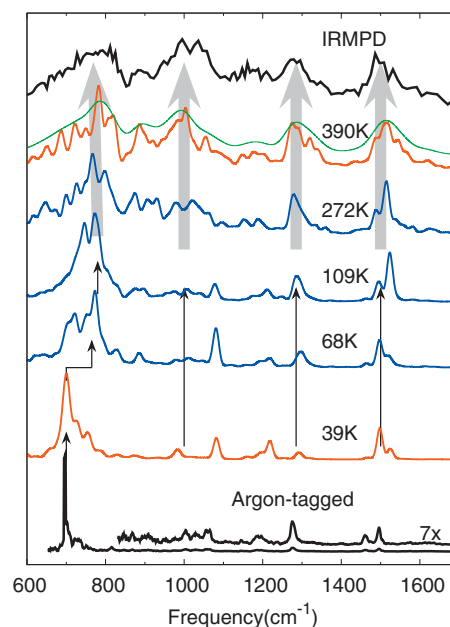

FIG. 3. The progression of finite temperature AIMD spectra for [Me$_2$O–D–OMe$_2$]$^+$ obtained using the $\alpha_\mu^{QC}(\omega)$ intensities of Eq. (3). As displayed in Fig. 2, the 39 K result (red) reproduces the argon-tagged spectrum well whereas the 390 K result (red) reproduces the IRMPD spectrum. The AIMD spectra at intermediate temperatures (blue) "interpolate" between the two experimental results. (Fluctuations in simulation temperature and other computational details are presented in Table I.) Note that the primary peak at 39 K shifts at 68 K and then dominates at higher temperatures. All spectra are filtered in frequency domain using a Gaussian with full width at half maximum of ≈15.3 cm^{-1}. On account of rotational broadening (see text) spectrum filtered using full width at half maximum about 50 cm^{-1} (green trace) is also provided.
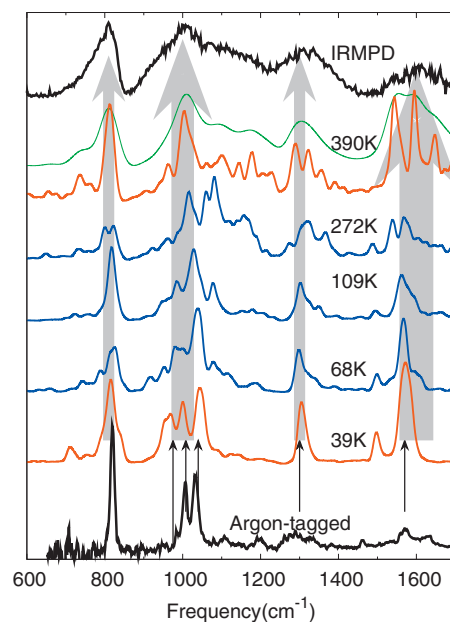

FIG. 4. The progression of finite temperature AIMD spectra for [Me$_2$O–H–OMe$_2$]$^+$ obtained using the $\alpha_\mu^{QC}(\omega)$ intensities of Eq. (3). Notice that the blueshift seen in the deuterated species is not present here. Fluctuations in simulation temperature and other computational details are presented in Table I. All spectra are filtered in the frequency domain using a Gaussian with full width at half maximum of ≈15.3 cm^{-1}. On account of rotational broadening (see text) spectrum filtered using full width at half maximum of about 50 cm^{-1} (green trace) is also provided.

dependent AIMD spectra are provided. In Ref. 31, we discussed the relationships between the 68 K AIMD spectra and the argon-tagged results and those between the 272 K AIMD spectra and the IRMPD results. Here we have also included results at 39, 109, and 390 K to provide a description of the spectral evolution that is consistent with that provided for the deuterated case here. Clearly, the peak positions in Fig. 4, obtained from the 39 K simulation match the low-temperature experimental results. The peaks at ~ 1000 cm^{-1} are reproduced here. Upon inspection of Fig. 1, it is clear that this triplet is not recovered by the harmonic spectrum. This aspect is reminiscent of the Zundel cation[21] since the reason for the splitting at 1000 cm^{-1} for the argon-tagged spectrum is due to the coupled motion of the shared proton stretch and methyl wag.[31] Furthermore, as the temperature is increased from 39 to 68 K, the triplet takes the form of a doublet with a shoulder on the red side of 1000 cm^{-1}. This also maintains qualitative similarity with the low-temperature experiment but as the temperature is increased even further, all spectral patterns including the feature at 1000 cm^{-1} become broad. However there are no spectral shifts like that seen for the deuterated case.

All AIMD spectra here have been filtered (or convoluted) in the frequency domain using a Gaussian with full width at half maximum of approximately 15.3 cm^{-1}. A major contribution to the linewidth in the IRMPD spectra arises from rotational broadening, which is not accounted for in the $J = 0$ simulations. Upon inspecting the narrowest feature in the IRMPD spectrum (the peak around 900 cm^{-1} in Fig. 2), we estimate this broadening to be approximately 50 cm^{-1}. To facilitate a consistent comparison between IRMPD and the theory, we have also convoluted the high-temperature AIMD spectra with a frequency domain Gaussian filter with full width at half maximum of approximately 50 cm^{-1}, which is represented using the green trace in Figs. 3 and 4. The convolution is found to smooth out some of the sharper features from the simulations, generally improving agreement with the IRMPD experiments. Note that this is only employed for the 390 K spectrum.

Some of the computed $\alpha_\mu^{QC}(\omega)$ intensities for higher frequencies are not in agreement with the experiments. While the $I_\mu^{QC}(\omega)$ intensities are in closer agreement with the argon-tagged spectrum [Fig. 2(a)], it was also noted in Ref. 31 that a probable reason for this discrepancy was due to the large density of harmonic mode states available to the system at the high-frequency range. More than a quarter of the 51 $[=(3N-6)]$ harmonic modes appear inside the 1450–1550 cm^{-1} window for the protonated species.[31] The role of these modes on the computed intensities is reconfirmed in Sec. IV B.

To summarize the results in Fig. 3 and 4, we note that while the simulated spectra of the proton-bound dimethyl ether dimer is generally broadened as a result of temperature, the deuterated species displays nontrivial changes with increasing temperature that include both growth in intensity as well as apparent spectral shifts. These spectral properties are analyzed in Secs. IV A and IV B.

IV. ROLE OF ENERGY REPARTITIONING ON TEMPERATURE DEPENDENCE

As discussed in Sec. III, the AIMD spectra agree reasonably well with all experimental results over a range of temperatures. For the experiments, the change in spectrum can be qualitatively understood from the temperature-dependent population of the vibrational eigenstates. At higher temperatures, excited vibrational states may be populated. Photon absorption from these excited states may lead to hot combination bands in the spectrum. To probe the reasons behind the change in the calculated dynamics spectra, we examine the energy repartitioning phenomena in our dynamics simulations by analyzing contributions from a basis of vibrational modes as a function of temperature. Specifically, two major factors are discussed. In Sec. IV B we analyze the blueshift in intensity in the 600–860 cm^{-1} region, for the shared deuteron, with an increase in temperature. We also discuss the effect of intensity borrowing on the computed spectrum. A theoretical analysis that allows these descriptions is provided below in Sec. IV A. It is important to note that while all the computational spectra are obtained using time-dependent AIMD trajectories, the interpretation of the spectra for the remaining portion of this publication are constructed in the frequency domain.

A. Decomposition of the finite temperature vibrational density of states

Energy redistribution in chemical systems has been well studied[56–68] in the past few decades. Influenced by the early work of Fermi *et al.*,[56,63] three of the present authors[31,69] formulated a scheme to decompose and assign the finite temperature vibrational density of states utilizing harmonic normal mode vectors that are obtained by diagonalizing the nuclear Hessian matrix at minimum energy. Briefly, consider the simulation time-averaged Fourier transform of the mass-weighted nuclear velocity vectors, $\vec{\mathcal{V}}(\omega)$, with the following elements:

$$\mathcal{V}_{i,j}(\omega) = \int_{t=0}^{t=T} dt \, \exp(-\iota \omega t) \widetilde{V}_{i,j}(t), \tag{5}$$

where $\widetilde{V}_{i,j}(t) \equiv (M_i^{1/2}/T) V_{i,j}(t)$ and $V_{i,j}(t)$ are elements of the velocity vector defined in Eq. (1). Using Parseval's theorem,[50] the time-averaged kinetic energy associated with the element (i,j) is given by

$$\bar{E}_{i,j} = \int_0^T dt |\widetilde{V}_{i,j}(t)|^2 = \int_0^\infty d\omega |\mathcal{V}_{i,j}(\omega)|^2. \tag{6}$$

The quantities $\vec{\mathcal{V}}(\omega)$ and $\vec{\widetilde{V}}(t)$ are first written as a linear combination of mass-weighted, orthonormal, complete, harmonic normal mode vectors, $\{\vec{H}_i\}$ as

$$\vec{\mathcal{V}}(\omega) = \sum_i C_i(\omega) * \vec{H}_i, \tag{7}$$

and

TABLE II. Measure of completeness of $(3N-6)$ $\vec{H}_i$ modes. The quantity ϵ_1 is unitless whereas ϵ_2 is in kcal/mol.

	[Me$_2$O–H–OMe$_2$]$^+$			[Me$_2$O–D–OMe$_2$]$^+$	
Temperature[a]	ϵ_1 [Eq. (14)]	ϵ_2 [Eq. (15)]	Temperature[a]	ϵ_1 [Eq. (14)]	ϵ_2 [Eq. (15)]
39 K ± 6 K	0.00137	0.0029	39 K ± 6 K	0.00157	0.0033
68 K ± 10 K	0.00174	0.0063	68 K ± 11 K	0.00140	0.0051
109 K ± 15 K	0.00190	0.0112	109 K ± 16 K	0.00176	0.0102
273 K ± 39 K	0.00922	0.1348	272 K ± 39 K	0.01034	0.1511
392 K ± 54 K	0.01056	0.2209	390 K ± 56 K	0.01423	0.2947

[a]Average temperature and fluctuations for all the AIMD and NVE simulations (in Kelvin).

$$\vec{\widetilde{V}}(t) = \sum_i \widetilde{C}_i(t) * \vec{H}_i, \tag{8}$$

with expansion coefficients, $C_i(\omega) = \vec{H}_i \cdot \vec{\mathcal{V}}(\omega)$ and $\widetilde{C}_i(t) = \vec{H}_i \cdot \vec{\widetilde{V}}(t)$, and $\widetilde{C}_i(t)$ is the inverse Fourier transform of $C_i(\omega)$. Since the AIMD dynamics trajectories conserve energy well, there is no center-of-mass translation during dynamics. Furthermore, due to conservation of angular momentum, free rotation is zero to within numerical precision (see Table I and associated discussion in Sec. II B).

Using Eq. (6), the kinetic energy of the system within a spectral range $[\omega_1, \omega_2]$ may be written as

$$\frac{1}{\omega_2 - \omega_1} \int_{\omega_1}^{\omega_2} d\omega \frac{1}{2} \vec{\mathcal{V}}(\omega) \cdot \vec{\mathcal{V}}(\omega)$$

$$= \frac{1}{\omega_2 - \omega_1} \int_{\omega_1}^{\omega_2} d\omega \left\{ \sum_i \frac{1}{2} |C_i(\omega)|^2 \right\}, \tag{9}$$

where the denominator $[\omega_2 - \omega_1]$ allows both sides of Eq. (9) to have units of energy. Thus Eq. (9) allows the introduction of a consistent energy partitioning scheme. Within this scheme, the net contribution of the ith normal mode to the kinetic energy and the vibrational density of states in the frequency range, $[\omega_1, \omega_2]$, is then written as a net sum of all its contributions inside the frequency range as

$$C_i^{[\omega_1, \omega_2]} = \left[\frac{1}{\omega_2 - \omega_1} \int_{\omega_1}^{\omega_2} d\omega |C_i(\omega)|^2 \right]^{1/2}$$

$$= \left[\frac{1}{\omega_2 - \omega_1} \int_{\omega_1}^{\omega_2} d\omega |\vec{H}_i \cdot \vec{\mathcal{V}}(\omega)|^2 \right]^{1/2}. \tag{10}$$

Since mass-weighted coordinates and velocities are used, the amount of energy in mode i in the range $[\omega_1, \omega_2]$ is $\frac{1}{2}\{C_i^{[\omega_1, \omega_2]}\}^2$. By contrast, the quantity $\frac{1}{2}|C_i(\omega)|^2$ represents the amount of energy in mode i at frequency ω. These aspects are clear from Eqs. (9) and (10), that is

$$\frac{1}{2} \sum_i \left[\frac{1}{\omega_2 - \omega_1} \int_{\omega_1}^{\omega_2} d\omega |C_i(\omega)|^2 \right] = \frac{1}{2} \sum_i \{C_i^{[\omega_1, \omega_2]}\}^2. \tag{11}$$

The relative $C_i^{[\omega_1, \omega_2]}$ contributions arising from the various AIMD simulations,

$$\frac{C_i^{[\omega_1, \omega_2]}}{\sqrt{\Sigma_i \{C_i^{[\omega_1, \omega_2]}\}^2}} = \sqrt{\frac{\frac{1}{2}\{C_i^{[\omega_1, \omega_2]}\}^2}{\sum_i \frac{1}{2}\{C_i^{[\omega_1, \omega_2]}\}^2}}$$

$$\equiv \sqrt{\frac{\text{kinetic energy in } i\text{th mode}}{\text{total kinetic energy}}}, \tag{12}$$

are compared in Sec. IV A 1. Since the dynamics is studied at multiple temperatures, by maintaining a constant $\{\vec{H}_i\}$ for all simulations, the change in the $C_i^{[\omega_1, \omega_2]}$ coefficients with temperature will yield insight on the contribution from a given mode i. By studying the temperature dependence of $C_i^{[\omega_1, \omega_2]}$ and the appropriate dipole weighted analog,

$$D_i^{[\omega_1, \omega_2]} = I_i^{1/2} * C_i^{[\omega_1, \omega_2]}, \tag{13}$$

with IR intensities I_i for the ith mode (computed within the harmonic approximation), important insight into the temperature-dependent intramolecular vibrational energy redistribution and partitioning is obtained in Sec. IV A 1. In practice, ω_1 and ω_2 are chosen to cover the relevant spectral feature. This is determined upon inspection of both the computed and experimental spectra.

1. Issue of completeness and choice of basis

It must further be noted that all analyses performed in Sec. IV B use the harmonic modes obtained at equilibrium geometry. However, in a dynamics simulation, anharmonicity is sampled and hence the moment of inertia tensor is not a constant and is asymmetrically sampled. As a result when only $(3N-6)$ internal modes are used for the decomposition in Eqs. (7) and (10), one expects a degree of incompleteness in the projection depicted by Eqs. (7) and (8). (There is, of course, no incompleteness when all $3N$ modes are used.) To quantify the incompleteness in such an analysis we compute,

$$\epsilon_1 = \frac{1}{T} \int dt \left\{ \frac{\vec{\widetilde{V}}(t) \cdot \vec{\widetilde{V}}(t) - \Sigma_i^{(3N-6)} |\widetilde{C}_i(t)|^2}{\vec{\widetilde{V}}(t) \cdot \vec{\widetilde{V}}(t)} \right\} \tag{14}$$

and

$$\epsilon_2 = T \int dt \left\{ \vec{\widetilde{V}}(t) \cdot \vec{\widetilde{V}}(t) - \sum_i^{(3N-6)} |\widetilde{C}_i(t)|^2 \right\}, \tag{15}$$

and present these in Table II. These quantities represent the relative and absolute loss in kinetic energy due to a decomposition that involves only $(3N-6)$ internal $\{\vec{H}_i\}$ mode vectors. The integrands in the equations above are always

greater than or equal to zero. As can be seen from Table II, the errors are small, but the fact that these numbers are not zero warrants a discussion. The higher temperature AIMD simulations deviate farther from the equilibrium geometry and hence the $\vec{\mathcal{V}}(\omega)$ vectors and the $\vec{\mathcal{V}}(t)$ vectors are not completely described by the (3N–6) internal $\{\vec{H}_i\}$ mode vectors obtained from a single minimum energy geometry. Indeed, the moment of inertia is not constant during the dynamics and fluctuates to a greater extent in the larger temperature simulations. However, the extent of incompleteness of the (3N–6) internal modes constructed at the equilibrium geometry is numerically negligible for all simulations discussed here and hence this factor is not considered further.

B. Analysis of energy repartitioning in the AIMD spectra

We first analyze the differences between the H and D spectra in the 600–860 cm^{-1} region. Toward this we decompose the finite temperature AIMD spectra in terms of the intrinsic harmonic normal modes, as outlined in Sec. IV A. In other words, we now utilize the harmonic mode vectors, $\{\vec{H}_i\}$, from Eq. (7), as a basis to decompose the mass-weighted nuclear velocity vectors, $\vec{\mathcal{V}}(\omega)$, to obtain an interpretation of the differences in the 600–860 cm^{-1} region.

The relative energy or relative-$C_i^{[\omega_1,\omega_2]}$ contributions [Eq. (12)] of the major harmonic modes in this spectral range are depicted in Figs. 5(a) and 5(b) as a function of simulation temperature. (Fig. 6 defines the critical modes seen in Fig. 5.) Figure 5(a) shows the temperature dependence of relative contribution defined in Eq. (12) for the major harmonic modes to the AIMD simulations in the 600–860 cm^{-1} region for [Me$_2$O–D–OMe$_2$]$^+$, while Figs. 5(b) displays the same for [Me$_2$O–H–OMe$_2$]$^+$. As stated earlier $\frac{1}{2}|C_i^{[\omega_1,\omega_2]}|^2$ is *the amount of energy* in mode i in the frequency range $[\omega_1,\omega_2]$ [see Eq. (9)]. Thus, Figs. 5(a) and 5(b) represent the temperature-dependent relative energy content in all modes containing non-negligible contributions in the spectral range of 600–860 cm^{-1}.

There are two dominant modes for both the proton and deuteron-bound species. These are the symmetric and anti-symmetric combinations of the shared H/D stretch, the ether backbone symmetric stretch and the methyl wag. We represent these modes using notation $X_{freq}^{OXO_{A-S}-COC_{S-S}}$ and $X_{freq}^{X_{\parallel}-COC_{S-S}}$, respectively, in Fig. 5 and in further discussion below. The symbol "X" represents either hydrogen (H) or deuterium (D). The modes are shown using the solid black and red curves in Fig. 5.

We first note the crossover between the red and black curves in Fig. 5(a). This indicates a relative repartitioning of energy between the corresponding modes. As temperature increases, the absolute energy content in both dominant modes increases but the relative contribution of $D_{665}^{ODO_{A-S}-COC_{S-S}}$ decreases compared to mode $D_{861}^{D_{\parallel}-COC_{S-S}}$ up to the point that the order of contributions is altered [Fig. 5(a)]. The crossover between the red and black curves in Fig. 5(a) indicates a relative reordering in contribution from these modes and is consistent with the blueshift in intensity in the low frequency region with an increase in temperature in Fig.
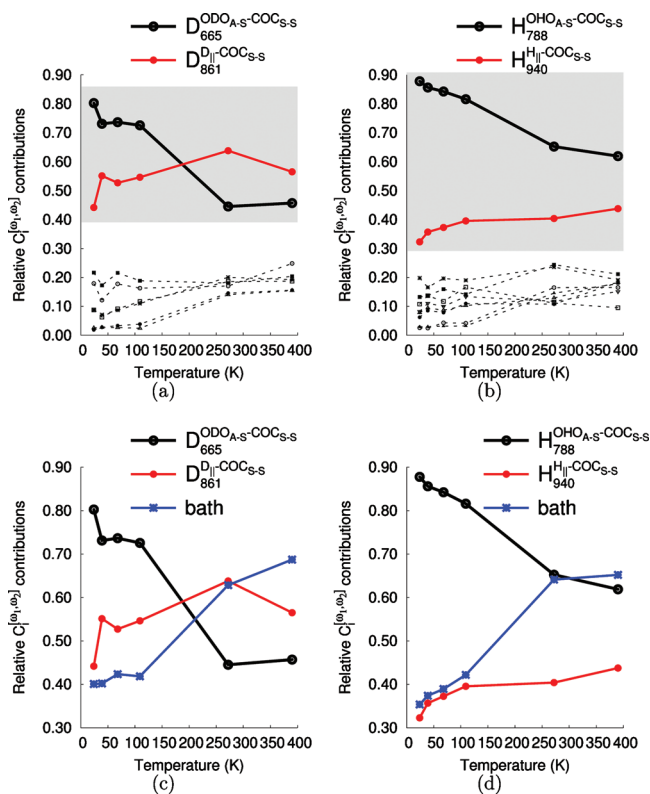

FIG. 5. Temperature-dependent energetic contributions from harmonic modes to the finite temperature AIMD spectra in the 600–860 cm^{-1} region. The relative $C_i^{[\omega_1,\omega_2]}$ [see Eq. (12)] contributions from significant modes for the (a) shared deuteron and (b) proton bound dimers are displayed (ω_1 =600 cm^{-1} and ω_2=860 cm^{-1}). The two dominant modes in these figures, $X_{freq}^{OXO_{A-S}-COC_{S-S}}$ and $X_{freq}^{X_{\parallel}-COC_{S-S}}$, where X is H/D and "freq" represents the frequency in wavenumber, are represented using solid red and black lines and are explained in Fig. 6. In (c) and (d) the cumulative contributions from all modes apart from $X_{freq}^{OXO_{A-S}-COC_{S-S}}$ and $X_{freq}^{X_{\parallel}-COC_{S-S}}$ are presented using the blue curve. These modes behave like bath mode that regulate energy flow (Refs. 70–72) between $X_{freq}^{OXO_{A-S}-COC_{S-S}}$ and $X_{freq}^{X_{\parallel}-COC_{S-S}}$. The relative $C_i^{[\omega_1,\omega_2]}$ contribution for the bath modes is defined as $\sqrt{\sum'_i|C_i^{[\omega_1,\omega_2]}|^2}$, the summation here excludes the contribution from the $X_{freq}^{OXO_{A-S}-COC_{S-S}}$ and $X_{freq}^{X_{\parallel}-COC_{S-S}}$ (and includes only the dashed lines from (a) and (b)).

3. This is a result of the fact that these modes are coupled by anharmonicity and is discussed further below.

We also note that a similar result is obtained upon inspection of the respective absolute $C_i^{[\omega_1,\omega_2]}$ contributions [Eq. (10)], which are shown in the supplementary material.[73]

How does this scenario differ from that found for the protonated dimer? Figure 5(b) indicates that the nature of modes that contribute significantly to the signature in the 600–860 cm^{-1} region for the shared proton system are essentially similar to that found in the shared deuteron system. That is in both cases, the motion in the 600–860 cm^{-1} region may be characterized by the mixing of the $X_{freq}^{OXO_{A-S}-COC_{S-S}}$ and $X_{freq}^{X_{\parallel}-COC_{S-S}}$ harmonic modes. One important distinction arises for the shared proton system through the fact that there is no reordering of contributions from the harmonic states like that seen for deuteron-bound dimer in Fig. 5(a). Compare the fact that the black and red curves cross in Figs. 5(a), thus changing the ordering of contributions; this does not happen for the protonated system in Figs. 5(b). An important reason for this is that there is minimal change in the relative $C_i^{[\omega_1,\omega_2]}$ contributions arising from
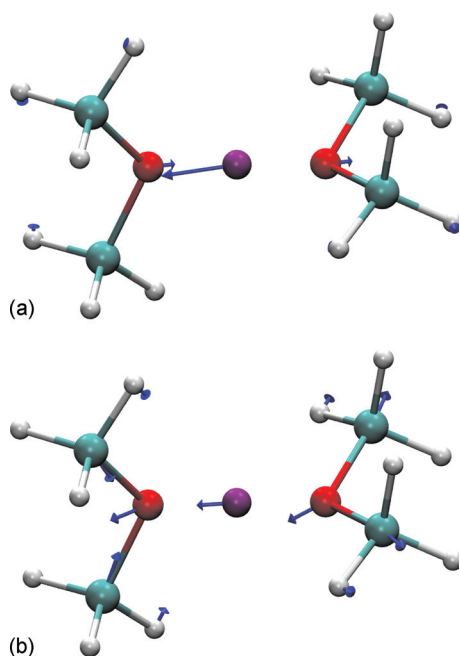
FIG. 6. (a) displays $X_{freq}^{OXO_{A-S}-COC_{S-S}}$, where X is H/D and freq represents the frequency in wavenumber, and the superscript represents the harmonic mode (eigenvector of the Hessian) corresponding to the coupled antisymmetric stretch of the OXO triatom with the symmetric stretch COC triatomic stretch. [URL: http://dx.doi.org/10.1063/1.3430525.1] (b) displays $X_{freq}^{X_{\parallel}-COC_{S-S}}$ and corresponds to the parallel H/D motion with the symmetric stretch COC triatomic stretch. Note that these two modes have significant contributions in Fig. 5. Notice that the displacements have been mass weighted. In both cases the shared H/D are shown in purple (enhanced online). [URL: http://dx.doi.org/10.1063/1.3430525.1]

$H_{940}^{H_{\parallel}-COC_{S-S}}$ in Fig. 5(b). Thus the relative reduction in contribution from $H_{788}^{OHO_{A-S}-COC_{S-S}}$ [indicated by the negative slope of the black curve in Fig. 5(b)] is compensated by an increase in contributions from many "bath" modes, where the bath modes are defined as all modes apart from $H_{788}^{OHO_{A-S}-COC_{S-S}}$ and $H_{940}^{H_{\parallel}-COC_{S-S}}$. This aspect is also clear from Figs. 5(c) and 5(d) where the $C_i^{[\omega_1,\omega_2]}$ contributions from the bath modes are presented using the blue curve. In Fig. 5(c), there is an energy redistribution between $D_{665}^{ODO_{A-S}-COC_{S-S}}$, $D_{861}^{D_{\parallel}-COC_{S-S}}$, and the bath modes. However, for the protonated species, the relative reduction in energy in $H_{788}^{OHO_{A-S}-COC_{S-S}}$ is almost completely absorbed by the bath modes. [Note that while contributions from the bath (blue) and $D_{861}^{D_{\parallel}-COC_{S-S}}$ (red) increase with temperature in Fig. 5(c), only contributions from the bath (blue) increase in Fig. 5(d).]

In the higher frequency regions, the argon-tagged action spectrum as well as the harmonic spectral results in Fig. 1 show very little intensity, while IRMPD provides much more structure. To further probe the reason for this spectral broadening in the high-frequency regions, we provide the $C_i(\omega)$ contributions [Eq. (7)] from $D_{665}^{ODO_{A-S}-COC_{S-S}}$ [Fig. 7(a)], $D_{861}^{D_{\parallel}-COC_{S-S}}$ [Fig. 7(b)], $H_{788}^{OHO_{A-S}-COC_{S-S}}$ [Fig. 8(a)], and $H_{940}^{H_{\parallel}-COC_{S-S}}$ [Fig. 8(b)]. We note that while the $C_i(\omega)$ contributions remain relatively localized in the frequency domain at lower temperatures, the contributions from the bright mode $D_{665}^{ODO_{A-S}-COC_{S-S}}$ broadens and extends over the entire spectral range when temperature is increased. In fact, the $C_i(\omega)$ contribution from $D_{665}^{ODO_{A-S}-COC_{S-S}}$ at 390 K is almost

identical to the IRMPD spectrum provided in Fig. 1(b). Since $D_{665}^{ODO_{A-S}-COC_{S-S}}$ is the only bright mode in the deuterated system, the higher frequency regions of the spectrum are generated by intensity borrowing. Thus there appears a close parallel between the temperature-dependent spectral broadening phenomenon noted here, that is facilitated by the wider sampling of anharmonicity on the potential surface, and temperature-dependent spectral diffusion in condensed phases where the energy deposited in a particular mode gets redistributed into the bath modes. For the shared proton system, the number of bright modes is greater and hence there are contributions to the spectrum that arise from each of the bright modes with an increase in temperature. It is also useful to note that while the contributions from the bath modes are qualitatively similar in Figs. 7 and 8, there are large contributions that arise for both cases in the higher frequency range. This coincides with the region of the spectrum in Figs. 3 and 4, where the $\alpha_\mu^{QC}(\omega)$ intensities obtained from AIMD are not in good agreement with experiment, more for the shared proton case than for the shared deuteron case. Since some of the bath modes have significant IR intensities[31] for the shared proton case, the larger contribution from these modes in the higher frequency region, particularly at high temperatures, gives rise to a significant contribution in Fig. 4.

In Fig. 9 we analyze the relative energy contributions as defined in Eq. (12) from the harmonic modes as a function of temperature in the higher frequency regions. As is clear from this figure, there are two different kinds of modes that contribute in any given spectral range: (a) the "in-band" harmonic modes that belong to the spectral range being analyzed, i.e., these belong inside the range $[\omega_1, \omega_2]$ in Eq. (10) and (b) the "out-of-band" harmonic modes that are outside the spectral range or outside $[\omega_1, \omega_2]$ in Eq. (10). At lower temperatures the contribution from the in-band harmonic modes is always well separated from the out-of-band modes. As temperature increases, the in-band and out-of-band modes begin to mix giving rise to a greater spread in energy and associated broadening of the vibrational spectrum. When the out-of-band mode is a bright mode as is the case for $D_{665}^{ODO_{A-S}-COC_{S-S}}$, this results in intensity borrowing into the dark modes in the high-frequency regions, as already noted from Fig. 7(a). Consequently, the "bright in-band" bonds are noted in green and the "bright out-of-band" that lead to intensity borrowing are shown in red in Fig. 9.

Using Fig. 9(a) we also provide an assignment for the broad feature in the 860–1050 cm^{-1} region in the low-temperature spectrum in Table III (see discussion in Sec. III). This region mostly has contributions from dark modes involving the motion of the shared deuteron along and orthogonal to the oxygen-oxygen axis coupled symmetric COC stretch and methyl wag. Spectral intensity is provided through contributions from the bright $D_{665}^{ODO_{A-S}-COC_{S-S}}$ mode.

A few comments are in order with respect to the temperature-dependent energy repartitioning among the harmonic mode vectors outlined above. As noted in Sec. IV A, the harmonic modes have been considered as a basis to describe the anharmonic motions encountered in AIMD. As the degree of anharmonicity increases, the elements of this bases
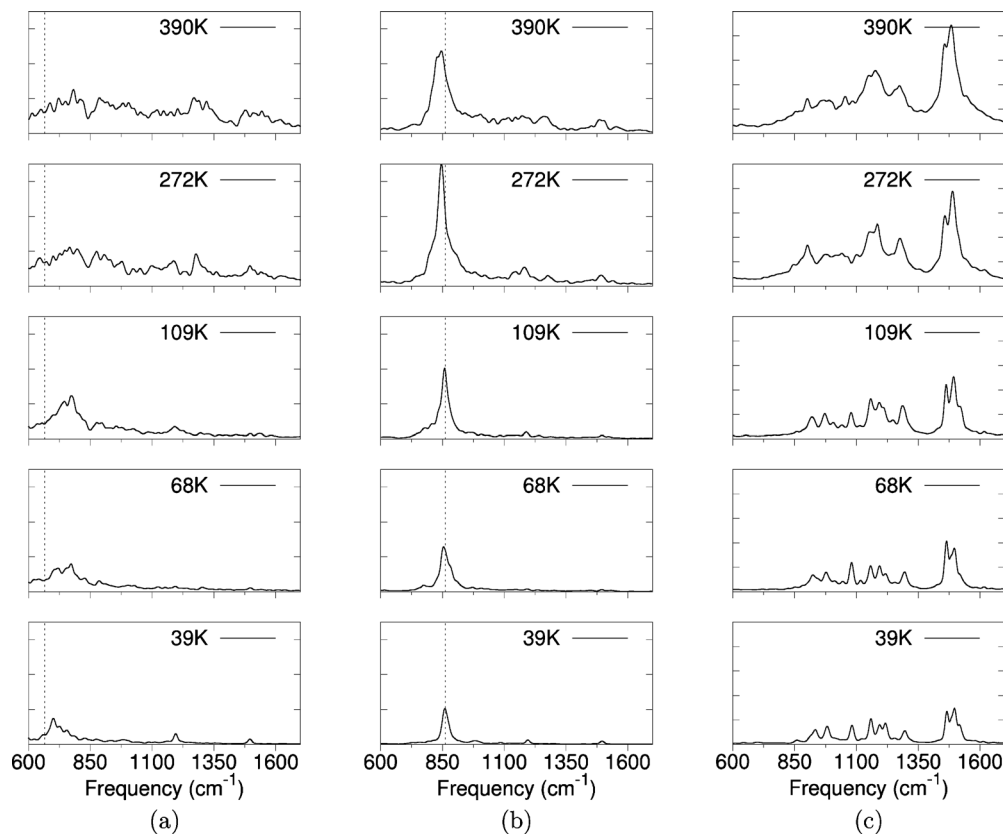
FIG. 7. The $C_i(\omega)$ contributions, computed using Eq. (7), from $D_{665}^{ODO_{A-S}-COC_{S-S}}$ (a) and $D_{861}^{D_\parallel-COC_{S-S}}$ (b) to the deuterated spectrum. The summed contribution from the bath modes [corresponding to the blue traces from Fig. 5(c)] is shown in (c). For (a) and (b), the corresponding harmonic frequencies are shown using a dotted vertical lines. The vertical axes in all figures have a uniform scale with a maximum value of 3.14 $(kcal/mol)^{1/2}$ for (a) and (b) and 11 $(kcal/mol)^{1/2}$ for (c). Note that the "spectral delocalization" of (a) $D_{665}^{ODO_{A-S}-COC_{S-S}}$ is unique and not seen for the other modes [compare with (b) and with Figs. 8(a) and 8(b), which depict the behavior of the corresponding modes in the shared proton system].

couple, giving rise to the temperature-dependent trends shown in Figs. 5, 7, and 8. Since the modes representing relative motion are reasonably complete (see Table II), these provide a numerically complete description of the dynamics data, which includes anharmonicity to all orders within the constraints of finite temperature dynamics. Furthermore, as temperature increases, two kinds of areas on the potential are sampled. (a) New local minima that were not populated at lower temperatures: This is important for many fluxional systems, such as those studied in Refs. 9, 30, 32, 45, and 46. However for the system considered here, this is not a factor since multiple optimization calculations beginning from different snapshots chosen from low and high-temperature dynamics suggest that there is only one contributing minimum. (b) Greater sampling of anharmonicity at each local minimum:[74] As temperature is increased the anharmonic regions sampled increase and vibrational hot bands appear at higher temperatures. In both cases, the region of potential sampled at higher temperatures acts as a perturbation to those sampled at lower temperatures and this further changes the coupling weights seen in Figs. 5. This explains the appearance of additional bands in the spectrum as temperature is increased in this treatment.

V. ANALYSIS OF REDUCED DIMENSIONAL DISTRIBUTION FUNCTIONS

To further probe the energy redistribution and coupled motion of the two fundamental modes shown in Fig. 6, we consider the projected motions along the two normal coordinates, $X_{freq}^{OXO_{A-S}-COC_{S-S}}$ and $X_{freq}^{X_\parallel-COC_{S-S}}$, using the AIMD trajectory data. In Fig. 10, we show the configurational distribution and Boltzmann averaged potential in the reduced two-dimensional phase space where the axes represent directions along the two chosen normal mode vectors for the case of the shared deuteron. To obtain these figures, the 3N-dimensional Cartesian coordinates at each dynamics step were projected onto the two normal mode axes as

$$H_{D_{665}^{ODO_{A-S}-COC_{S-S}}} \cdot \vec{\mathcal{R}}(t) \tag{16}$$

and

$$H_{D_{861}^{D_\parallel-COC_{S-S}}} \cdot \vec{\mathcal{R}}(t), \tag{17}$$

where $\vec{\mathcal{R}}(t)$ represents the mass-weighted coordinates obtained from the AIMD trajectory. The quantities $H_{D_{665}^{ODO_{A-S}-COC_{S-S}}}$ and $H_{D_{861}^{D_\parallel-COC_{S-S}}}$ represent the mass-weighted harmonic mode vectors along $D_{665}^{ODO_{A-S}-COC_{S-S}}$ and $D_{861}^{D_\parallel-COC_{S-S}}$, respectively. The resultant data were used to obtain a reduced dimensional distribution function that is averaged over all other coordinates (central column of Fig. 10). This central column indicates that at low temperatures, the motions along the two modes are strongly correlated [verified by the tilted diagonal distribution in Fig. 10(a)]. It is further noted that as the temperature increases, the two
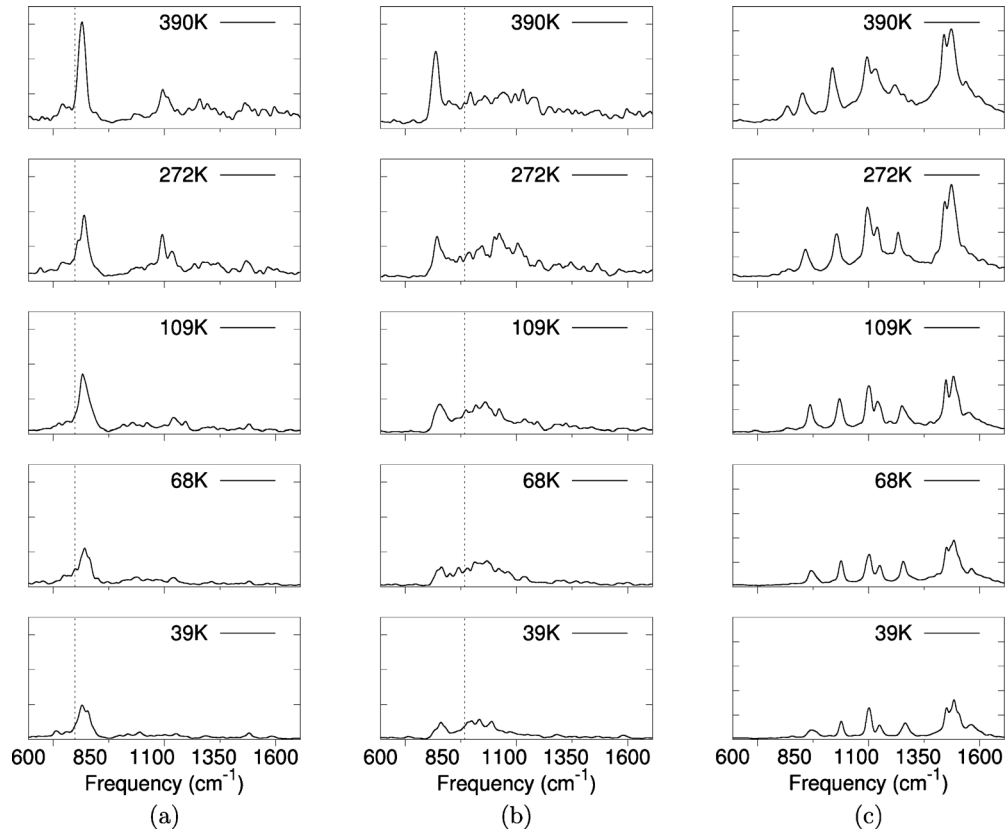
FIG. 8. The $C_i(\omega)$ contributions, computed using Eq. (7), from (a) $H_{788}^{OHO_{A-S}-COC_{S-S}}$ and (b) $H_{940}^{H_{\parallel}-COC_{S-S}}$ to the protonated spectrum. The summed contribution of the bath modes [corresponding to the blue traces from Fig. 5(d)] are shown in (c), and are observed to be qualitatively similar at all temperatures for H and D [compare with Fig. 7(c)]. (a) and the corresponding harmonic frequencies are shown using dotted vertical lines. The vertical axis in all figures has a uniform scale with a maximum value of 3.14 $(kcal/mol)^{1/2}$ for (a) and (b) and 11 $(kcal/mol)^{1/2}$ for (c).

modes get uncorrelated and the distribution becomes uniform [Figs. 10(b) and 10(c)].

To confirm this qualitative trend we probe this effect by computing reduced dimensional quantum distribution functions. To obtain the quantum nuclear distribution, eigenstates are calculated and presented on the rightmost column in Fig. 10. The eigenstates correspond to the two-dimensional Hamiltonian described in the coordinate representation as

$$H(\{x_{i_I}^I, x_{j_I}^I\}) = -\sum_{I=1}^{2} \frac{\hbar^2}{2} \tilde{K}(x_{i_I}^I, x_{j_I}^I) + V(x_{i_1}^1, x_{i_2}^2) \delta_{x_{i_1}^1, x_{j_1}^1} \delta_{x_{i_2}^2, x_{j_2}^2},$$
(18)

where $\{x_{i_I}^I\}$ is the coordinate representation of the two mass-weighted modes in Fig. 10, depicted using the index I and the kinetic energy operator $\tilde{K}(x_{i_I}^I, x_{j_I}^I)$ is represented in each mass-weighted dimension using distributed approximating functionals,[75–78]

$$\tilde{K}(x_i, x_j) = \frac{1}{\sigma\sqrt{2\pi}} \left(\frac{-1}{\sqrt{2}\sigma} \right)^2 \exp\left(-\frac{(x_i - x_j)^2}{2\sigma^2} \right)$$

$$\times \sum_{n=0}^{M/2} \left(\frac{-1}{4} \right)^n \frac{1}{n!} H_{2n+k}\left(\frac{x_i - x_j}{\sqrt{2}\sigma} \right).$$
(19)

The H_{2n+k} are Hermite polynomials. The potential energy,

$$V(x_i^1, x_j^2) \equiv \langle V(x_i^1, x_j^2; \mathbf{R_C}) \rangle_{\mathbf{Q_C}},$$
(20)

represents the reduced dimensional potential energy surface computed from the ensemble averaged classical AIMD data (left column of Fig. 10), constructed the same way as the classical distribution functions shown in the central column of Fig. 10. The subscript $\mathbf{Q_C}$ represents the fact that all other coordinates orthogonal to $X_{freq}^{OXO_{A-S}-COC_{S-S}}$ and $X_{freq}^{X_{\parallel}-COC_{S-S}}$ are averaged to obtain the reduced dimensional potential. The Hamiltonian in Eq. (18) is diagonalized using an efficient iterative Arnoldi iterative diagonalization scheme[31,74,79–82] to obtain the lowest quantum eigenstates. The resultant eigenstates from Eq. (18) are used to make qualitative comparisons with the classical distribution.

The resultant quantum zero-point eigenstates are shown on the right column of Fig. 10. These modes are essentially the coupled anharmonicity corrected modes in this two-dimensional representation. The correlated behavior discussed above is generally consistent between the classical and quantum treatments. That is, in both cases the low-temperature distribution shows that the two modes are correlated and this is displayed by the tilted diagonal distribution for the 39 and 68 K results in Fig. 10. In addition, the delocalization is roughly comparable in both cases. However, there are differences between the quantum and classical distributions as well such as the orthogonal spread in the top two panels of Fig. 10 and the difference in confinement in the bottom panels. While these differences do not change the
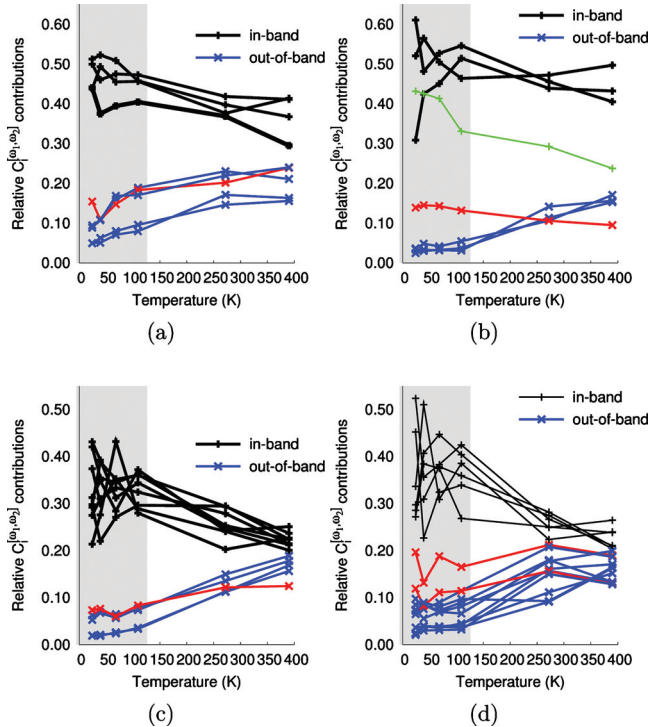
FIG. 9. The temperature-dependent intensity contributions from harmonic modes to the AIMD spectra of (a) $[Me_2O-\mathbf{D}-OMe_2]^+$ in the (b) $860-1060$ cm^{-1} region, (c) $1060-1240$ cm^{-1} region, and of (b) $[Me_2O-\mathbf{H}-OMe_2]^+$ $860-1060$ cm^{-1} region, (d) $1060-1240$ cm^{-1}. In all the displayed spectral regions, the in-band modes (that are the harmonic modes inside the chosen spectral region, which is inside the range $[\omega_1,\omega_2]$) always have higher contributions at lower temperatures. In fact, in most cases there is a clear separation in contributions arising from the in-band and out-of-band modes (modes outside the chosen spectral region that is outside the range $[\omega_1,\omega_2]$) as seen in the shaded region of the plots. An increase in temperature facilitates energy transfer between these modes. To highlight the contributions, the out-of-band bright modes are shown in red, while the in-band bright modes are in green.

qualitative result that shows how the two modes are correlated at lower temperatures, a detailed analysis of the differences between the quantum and classical distributions will be conducted in a future publication.[83]

VI. CONCLUDING REMARKS

In this publication we have investigated the temperature-dependent effects of H/D isotopic substitution on an organic dimer bound with a short, strong hydrogen bond, using mul-

tiple experimental and computational techniques. The critical interactions involved in the systems studied here are also seen in many host-guest systems,[22] where hydrogen bond modulation allows complex molecular hosts to selectively bind a variety of molecular guests. Similar systems have been used as models to understand the role of secondary isotope substitution in modulating vibrational energy flow in enzyme active sites.[23] When the R-group is a hydrogen atom, the system studied represents the well-known Zundel cation,[18–21] which plays an important role in proton transfer in condensed phase systems.

We find that when the proton in the intermolecular hydrogen bond is exchanged by a deuteron, qualitative changes are observed in the infrared spectra across a broad range of temperatures. The AIMD simulations reveal that for both isotopologues, the temperature-dependent changes in the spectra can be understood in terms of increased sampling of the anharmonic regions of the potential energy surface with increasing temperature. Harmonic decomposition analysis further reveals that the qualitatively different trends observed upon isotopic substitution can be understood in terms of the different mode couplings in the H- and D-bound systems.

A key result of this work is that we have shown that a single potential energy surface is sufficient to computationally reproduce measured vibrational spectra recorded at different temperatures using different experimental schemes, including the effects of isotopic substitution, with temperature as the only independent parameter. This speaks to the robustness of the AIMD method for this sort of study, and shows that it can be a valuable tool for understanding complicated spectra that are not amenable to analysis using typical methods. Furthermore, the harmonic decomposition techniques applied here allowed us to examine the changes in the contributions of the various normal modes in different spectral regions as a function of temperature, and thereby to understand the observed differences between the spectra of the H- and D-bound systems. Specifically, the normal modes involving the stretching motion of the intermolecular H/D-bond, labeled $X^{OXO_{A-S}-COC_{S-S}}_{freq}$ and $X^{X_{\parallel}-COC_{S-S}}_{freq}$, show drastically different behaviors. In the deuteron-bound case, virtually all of the infrared intensity is carried by a single mode $D^{ODO_{A-S}-COC_{S-S}}_{665}$, which starts out as a spectrally localized peak at low temperatures, but rapidly becomes delocalized with increasing temperature, until at 390 K it extends

TABLE III. Analysis of the vibrational harmonic frequency components that contribute in the $860-1060$ cm^{-1} region at 39 and 68 K. The $C_i^{[\omega_1,\omega_2]}$ and $D_i^{[\omega_1,\omega_2]}$ decomposition coefficients are provided; $D_i^{[\omega_1,\omega_2]}$ inside parenthesis.

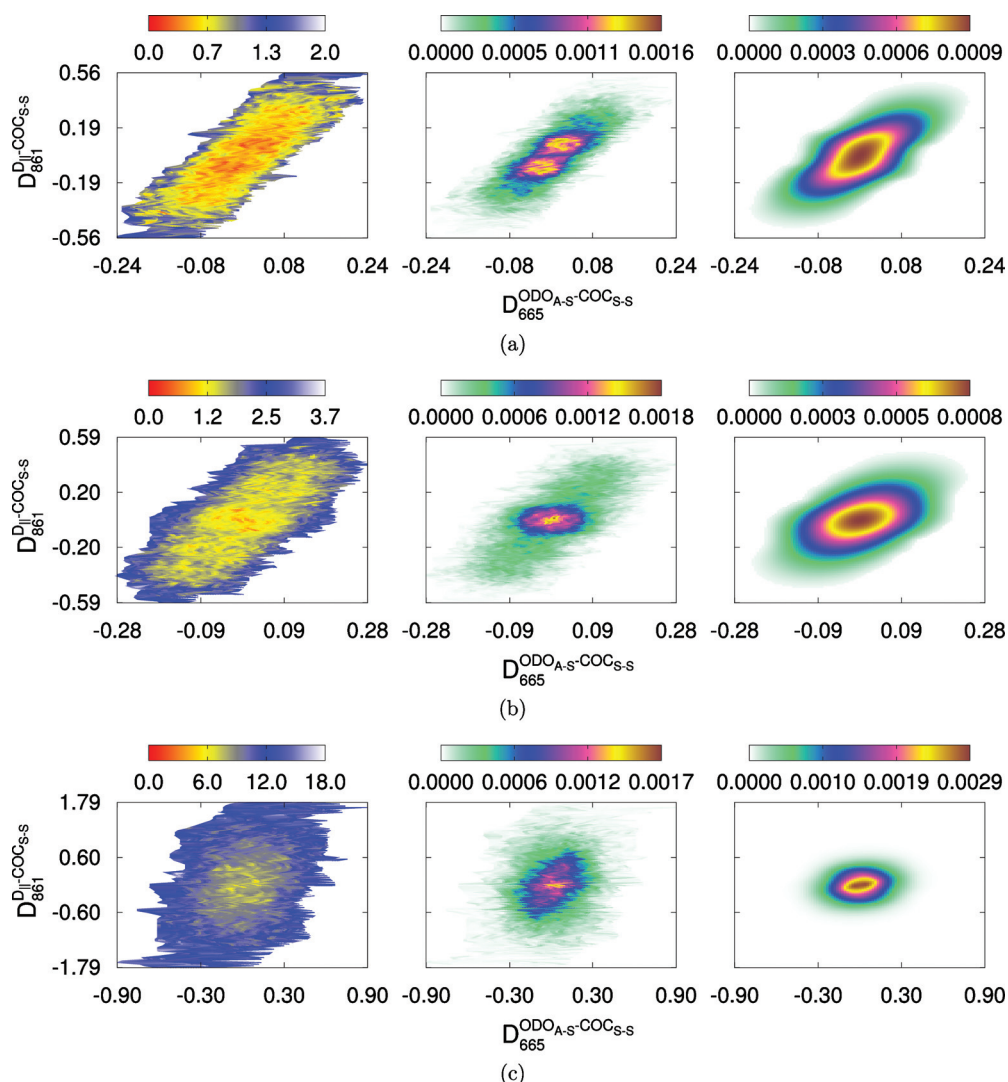|	Harmonic mode decompositions in the region $860-1060$ cm^{-1}
39 K	$\dfrac{0.71}{(0.63)} D^{D_{\perp}-COC_{A-S}}_{987} + \dfrac{0.55}{(0.06)} D^{D_{\perp}-COC_{S-S}}_{929} + \dfrac{0.27}{(0.10)} D^{D_{\parallel}-COC_{S-S}}_{861} + \dfrac{0.16}{(0.18)} D^{D_{\perp}-COC_{A-S}-CH3_{rock}}_{1082}$ $+ \dfrac{0.11}{(0.04)} D^{CH3_{rock}}_{1194} + \dfrac{0.11}{(0.72)} D^{ODO_{A-S}-COC_{S-S}}_{665}$
68 K	$\dfrac{0.69}{(0.50)} D^{D_{\perp}-COC_{A-S}}_{987} + \dfrac{0.52}{(0.05)} D^{D_{\perp}-COC_{S-S}}_{929} + \dfrac{0.31}{(0.10)} D^{D_{\parallel}-COC_{S-S}}_{861} + \dfrac{0.25}{(0.23)} D^{D_{\perp}-COC_{A-S}-CH3_{rock}}_{1082}$ $+ \dfrac{0.14}{(0.81)} D^{ODO_{A-S}-COC_{S-S}}_{665}$

FIG. 10. Reduced dimensional potential (left column) and reduced dimensional configurational distribution function for classical (central column) and quantum (right column) treatments of the shared deuteron in the deuteron-bound systems at temperatures (a) 39 K, (b) 68 K, and (c) 272 K. Potential energy is in kcal/mol. The horizontal axis represents the span along the normal, mass-weighted coordinates $D_{665}^{ODO_{A-S}-COC_{S-S}}$, whereas the vertical axis represents motion along the $D_{861}^{D_{\parallel}-COC_{S-S}}$. This behavior is qualitatively similar for both systems. While there exist quantitative differences between the quantum and classical treatments, both treatments predict the correlated (mixed) description of the two modes shown as a result of breakdown of spherical symmetry of the potential at lower temperatures.

across the entire measured spectral region from 600 to 1600 cm^{-1}. On the other hand, the $D_{861}^{D_{\parallel}-COC_{S-S}}$ mode stays fairly localized in the spectrum at all temperatures. The analysis of the integrated contributions of these modes to the spectral region between 600–860 cm^{-1} indicates that there is temperature-dependent repartitioning of the energy in the $D_{665}^{ODO_{A-S}-COC_{S-S}}$ and $D_{861}^{D_{\parallel}-COC_{S-S}}$ modes, with the contribution from the latter becoming dominant at high temperatures. This "crossover" occurs at the same temperatures corresponding to a blueshift of the infrared band in the same spectral region, providing some evidence that the coupling between the 665 and 861 cm^{-1} modes may be responsible for the blueshift—a hypothesis which will be further investigated in a future publication. Moreover, the fact that these two modes are coupled through anharmonicity is confirmed through reduced dimensional quantum nuclear calculations, where the distribution functions are in agreement with the classical AIMD calculations.

The situation is completely different in the proton-bound case, where both the $H_{788}^{OHO_{A-S}-COC_{S-S}}$ and $H_{940}^{H_{\parallel}-COC_{S-S}}$ contribute to the spectral intensity at all temperatures. While these modes exhibit some spectral delocalization with increasing temperature, it is not nearly as pronounced as for the deuteron-bound case. This tends to suggest that the coupling between these modes is much less pronounced than in the D-bound system. One additional point is that both systems show qualitatively similar temperature-dependent trends for the weakly contributing bath modes.

Finally, there appears a parallelism between the temperature-dependent spectral broadening process seen here and the idea of spectral diffusion in condensed phases where energy deposited in a particular mode gets dissipated into the bath modes. The upshot of this analysis is that the strongly anharmonic nature of the intermolecular potentials in these proton-bound systems leads to facile coupling of the shared H/D stretch to the harmonic modes of the monomer back-

bones. As we have seen, this can lead to qualitatively different behavior upon deuteration, which has general ramifications for H–D exchange process.

ACKNOWLEDGMENTS

[1] Z. Nagel and J. Klinman, Chem. Rev. (Washington, D.C.) **106**, 3095 (2006).
[2] S. M. Haile, D. A. Boysen, C. R. I. Chisholm, and R. B. Merle, Nature (London) **410**, 910 (2001).
[3] B. S. Hudson and N. Verdal, Physica B **385–386**, 212 (2006).
[4] B. J. Gertner and J. T. Hynes, Science **271**, 1563 (1996).
[5] J. P. Devlin, N. Uras, J. Sadlej, and V. Buch, Nature (London) **417**, 269 (2002).
[6] J. S. Aloisio and S. Francisco, Acc. Chem. Res. **33**, 825 (2000).
[7] J. R. Roscioli, L. R. McCunn, and M. A. Johnson, Science **316**, 249 (2007).
[8] M. K. Petersen, S. S. Iyengar, T. J. F. Day, and G. A. Voth, J. Phys. Chem. B **108**, 14804 (2004).
[9] S. S. Iyengar, T. J. F. Day, and G. A. Voth, Int. J. Mass Spectrom. **241**, 197 (2005).
[10] W. W. Cleland and M. M. Kreevoy, Science **264**, 1887 (1994).
[11] P. A. Frey, S. A. Whitt, and J. B. Tobin, Science **264**, 1927 (1994).
[12] D. C. Chatfield and B. R. Brooks, J. Am. Chem. Soc. **117**, 5561 (1995).
[13] A. Warshel, A. Papazyan, and P. A. Kollman, Science **269**, 102 (1995).
[14] J. A. Gerlt, M. M. Kreevoy, W. W. Cleland, and P. A. Frey, Chem. Biol. **4**, 259 (1997).
[15] C. L. Perrin and J. B. Nielson, Annu. Rev. Phys. Chem. **48**, 511 (1997).
[16] A. Warshel and A. Papazyan, Proc. Natl. Acad. Sci. U.S.A. **93**, 13665 (1996).
[17] D. L. Harris, J. Inorg. Biochem. **91**, 568 (2002).
[18] E. G. Diken, J. M. Headrick, J. R. Roscioli, J. C. Bopp, M. A. Johnson, and A. B. McCoy, J. Phys. Chem. A **109**, 1487 (2005).
[19] N. I. Hammer, E. G. Diken, J. R. Roscioli, M. A. Johnson, E. M. Myshakin, K. D. Jordan, A. B. McCoy, X. Huang, J. M. Bowman, and S. Carter, J. Chem. Phys. **122**, 244301 (2005).
[20] K. R. Asmis, N. L. Pivonka, G. Santambrogio, M. Brmmer, C. Kaposta, D. M. Neumark, and L. Wöste, Science **299**, 1375 (2003).
[21] O. Vendrell, F. Gatti, and H.-D. Meyer, Angew. Chem., Int. Ed. **127**, 184303 (2007).
[22] G. Cooke and V. M. Rotello, Chem. Soc. Rev. **31**, 275 (2002).
[23] A. Kohen and J. Jensen, J. Am. Chem. Soc. **124**, 3858 (2002).
[24] G. J. Diebold, F. Engelke, D. M. Lubman, J. C. Whitehead, and R. N. Zare, J. Chem. Phys. **67**, 5407 (1977).
[25] E. R. Grant, M. J. Coggiola, Y. T. Lee, P. A. Schulz, Aa. S. Sudbo, and Y. R. Shen, Chem. Phys. Lett. **52**, 595 (1977).
[26] D. S. Bomse, R. L. Woodin, and J. L. Beauchamp, J. Am. Chem. Soc. **101**, 5503 (1979).
[27] J. J. Valle, J. R. Eyler, J. Oomens, D. T. Moore, A. F. G. van der Meer, G. von Helden, G. Meijer, C. L. Hendrickson, A. G. Marshall, and G. T. Blakney, Rev. Sci. Instrum. **76**, 023103 (2005).
[28] D. T. Moore, J. Oomens, L. van der Meer, G. von Helden, G. Meijer, J. Valle, A. G. Marshall, and J. R. Eyler, ChemPhysChem **5**, 740 (2004).
[29] T. D. Fridgen, P. MacAleese, L. Maitre, T. B. McMahon, P. Boissel, and J. Lemaire, Phys. Chem. Chem. Phys. **7**, 2747 (2005).
[30] S. S. Iyengar, J. Chem. Phys. **126**, 216101 (2007).
[31] X. Li, D. T. Moore, and S. S. Iyengar, J. Chem. Phys. **128**, 184308 (2008).
[32] X. Li, V. E. Teige, and S. S. Iyengar, J. Phys. Chem. A **111**, 4815 (2007).
[33] N. C. Polfer and J. Oomens, Mass Spectrom. Rev. **28**, 468 (2009).
[34] J. R. Eyler, Mass Spectrom. Rev. **28**, 448 (2009).
[35] J. Oomens, B. G. Sartakov, G. Meijer, and G. von Helden, Int. J. Mass Spectrom. **254**, 1 (2006).
[36] J.-W. Shin, N. I. Hammer, E. G. Diken, M. A. Johnson, R. S. Walters, T. D. Jaeger, M. A. Duncan, R. A. Christie, and K. D. Jordan, Science **304**, 1137 (2004).
[37] C. Leforestier, J. Chem. Phys. **68**, 4406 (1978).
[38] K. Bolton, W. L. Hase, and G. H. Peslherbe, *Modern Methods for Multidimensional Dynamics Computation in Chemistry* (World Scientific, Singapore, 1998), p. 143.
[39] M. C. Payne, M. P. Teter, D. C. Allan, T. A. Arias, and J. D. Joannopoulos, Rev. Mod. Phys. **64**, 1045 (1992).
[40] H. B. Schlegel, J. M. Millam, S. S. Iyengar, G. A. Voth, A. D. Daniels, G. E. Scuseria, and M. J. Frisch, J. Chem. Phys. **114**, 9758 (2001).
[41] S. S. Iyengar, H. B. Schlegel, J. M. Millam, G. A. Voth, G. E. Scuseria, and M. J. Frisch, J. Chem. Phys. **115**, 10291 (2001).
[42] H. B. Schlegel, S. S. Iyengar, X. Li, J. M. Millam, G. A. Voth, G. E. Scuseria, and M. J. Frisch, J. Chem. Phys. **117**, 8694 (2002).
[43] S. S. Iyengar, H. B. Schlegel, G. A. Voth, J. M. Millam, G. E. Scuseria, and M. J. Frisch, Isr. J. Chem. **42**, 191 (2002).
[44] M. J. Frisch, G. W. Trucks, H. B. Schlegel *et al.*, GAUSSIAN 03, Revision b.02, Gaussian, Inc., Pittsburgh PA, 2003.
[45] S. S. Iyengar, M. K. Petersen, T. J. F. Day, C. J. Burnham, V. E. Teige, and G. A. Voth, J. Chem. Phys. **123**, 084309 (2005).
[46] S. S. Iyengar, J. Chem. Phys. **123**, 084310 (2005).
[47] S. S. Iyengar and M. J. Frisch, J. Chem. Phys. **121**, 5061 (2004).
[48] D. Svozil and P. Jungwirth, J. Phys. Chem. A **110**, 9194 (2006).
[49] S. Sadhukhan, D. Munoz, C. Adamo, and G. E. Scuseria, Chem. Phys. Lett. **306**, 83 (1999).
[50] W. H. Press, S. A. Teukolsky, W. T. Vetterling, and B. P. Flannery, *Numerical Recipes in C* (Cambridge University Press, New York, 1992).
[51] R. G. Gordon, Adv. Magn. Reson. **3**, 1 (1968).
[52] D. A. McQuarrie, *Statistical Mechanics* (University Science Books, Sausalito, CA, 2000).
[53] P. H. Berens, S. R. White, and K. R. Wilson, J. Chem. Phys. **75**, 515 (1981).
[54] J. S. Bader and B. J. Berne, J. Chem. Phys. **100**, 8359 (1994).
[55] C. P. Lawrence, A. Nakayama, N. Makri, and J. L. Skinner, J. Chem. Phys. **120**, 6621 (2004).
[56] E. Fermi, J. R. Pasta, and S. Ulam, Los Alamos Technical Report No. 1940, 1955.
[57] *Unimolecular Reactions* (Wiley, New York, 1972).
[58] *Theory of Unimolecular Reactions* (Academic, New York, 1973).
[59] J. Jortner and R. Levine, Adv. Chem. Phys. **47**, 1 (1981).
[60] C. S. Parmenter, J. Phys. Chem. **86**, 1735 (1982).
[61] C. S. Parmenter, Faraday Discuss. Chem. Soc. **75**, 7 (1983).
[62] L. R. Khundkar and A. H. Zewail, Annu. Rev. Phys. Chem. **41**, 15 (1990).
[63] T. Uzer and W. H. Miller, Phys. Rep. **199**, 73 (1991).
[64] D. J. Nesbitt and R. W. Field, J. Chem. Phys. **100**, 12735 (1996).
[65] M. Gruebele, Theor. Chem. Acc. **109**, 53 (2003).
[66] Y. Liu, L. L. Lohr, and J. R. Barker, J. Phys. Chem. B **109**, 8304 (2005).
[67] S. Keshavamurthy, Int. Rev. Phys. Chem. **26**, 521 (2007).
[68] E. L. Sibert, W. P. Reinhardt, and J. T. Hynes, J. Chem. Phys. **81**, 1115 (1984).
[69] D. Vimal, A. B. Pacheco, S. S. Iyengar, and P. S. Stevens, J. Phys. Chem. A **112**, 7227 (2008).
[70] G. L. Barnes, S. M. Squires, and E. L. Sibert, J. Phys. Chem. B **112**, 595 (2008).
[71] W. H. Miller, N. C. Handy, and J. E. Adams, J. Chem. Phys. **72**, 99 (1980).

[72] K. Takahashi, K. L. Plath, R. T. Skodje, and V. Vaida, J. Phys. Chem. A **112**, 7321 (2008).

[73] See supplementary material at http://dx.doi.org/10.1063/1.3430525 for absolute $C_i^{[\omega_1, \omega_2]}$ contributions [Eq. (10)].

[74] I. Sumner and S. S. Iyengar, J. Phys. Chem. A **111**, 10313 (2007).

[75] S. S. Iyengar and J. Jakowski, J. Chem. Phys. **122**, 114105 (2005).

[76] S. S. Iyengar, Theor. Chem. Acc. **116**, 326 (2006).

[77] D. K. Hoffman, N. Nayar, O. A. Sharafeddin, and D. J. Kouri, J. Phys. Chem. **95**, 8299 (1991).

[78] D. J. Kouri, Y. Huang, and D. K. Hoffman, Phys. Rev. Lett. **75**, 49 (1995).

[79] J. Jakowski, I. Sumner, and S. S. Iyengar, J. Chem. Theory Comput. **2**, 1203 (2006).

[80] D. C. Sorensen, SIAM J. Matrix Anal. Appl. **13**, 357 (1992).

[81] G. H. Golub and C. F. van Loan, *Matrix Computations* (The Johns Hopkins University Press, Baltimore, 1996).

[82] B. N. Parlett and Y. Saad, Linear Algebr. Appl. **88–89**, 575 (1987).

[83] X. Li, D. T. Moore, and S. S. Iyengar (unpublished).